



# Create a strong internal electric-field on PDI photocatalysts for boosting phenols degradation via preferentially exposing $\pi$ -conjugated planes up to 100%

Yaning Zhang<sup>a,b</sup>, Dan Wang<sup>a,b</sup>, Weixu Liu<sup>d</sup>, Yang Lou<sup>a,b</sup>, Ying Zhang<sup>a,b</sup>, Yuming Dong<sup>a,b</sup>, Jing Xu<sup>c</sup>, Chengsi Pan<sup>a,b,\*</sup>, Yongfa Zhu<sup>a,b,d,\*</sup>

<sup>a</sup> Key Laboratory of Synthetic and Biological Colloids, Ministry of Education, School of Chemical and Material Engineering, Jiangnan University, Wuxi, Jiangsu, 214122, China

<sup>b</sup> International Joint Research Center for Photoresponsive Molecules and Materials, Jiangnan University, Wuxi, Jiangsu 214122, China

<sup>c</sup> School of Food Science and Technology, Jiangnan University, Wuxi 214122, PR China

<sup>d</sup> Department of Chemistry, Tsinghua University, Beijing 100084, China

## ARTICLE INFO

### Keywords:

PDI  
Internal electric field  
Facet control  
Photocatalyst  
Phenol

## ABSTRACT

Nearly 100% exposure of  $\pi$ -conjugated planes, whose structure inherently exhibits large electron delocalization and fast charge transfer, has been achieved in perylene diimide (PDI) supramolecular photocatalysts by a solvent-induced self-assembly method. The high exposure ratio of  $\pi$ -conjugated planes is found to cause a larger surface potential and higher surface charge density by experimental data, and higher electron distribution by DFT calculations, relative to  $\pi$ -stacked planes exposed on PDI nanorods or (020) planes exposed on PDI particles, resulting in a strong internal electric field. This gives  $\pi$ -conjugated PDI ca. 8–17 times higher activity on phenols photodegradation than reported PDI, and 4–6 times higher activity than well-known photocatalysts like  $\text{Bi}_2\text{WO}_6$  or  $\text{g-C}_3\text{N}_4$ . The successful control of PDI to preferentially expose  $\pi$ -conjugated planes may not only boost the photocatalytic activity in this system, but also give some guidelines in the design and development of more efficient organic photocatalysts with wide spectrum response.

## 1. Introduction

Phenol and its derivatives (catechol, bisphenol A (BPA), 4-chlorophenol (4-CP) and 2,4-chlorophenol (2,4-DCP)) are highly toxic contaminants that are frequently found in raw water and in industrial effluents. The pollutants tend to persist in the environment for a long time, and may cause internal and neurological diseases or cancer even in an extremely low concentration (ca. 10 ppm) [1,2]. Photocatalytic technology exhibits promising capability on the removal of such highly toxic compounds, with the advantage of sunlight utilization, completely mineralization and fully functional in a low-level concentration. But the technology is currently lack of ideal photocatalysts with sufficient solar energy utilization [3,4].

Organic photocatalysts have recently attracted much of interests because they can be designed by learning from tons of organic synthetic methods. Exemplar photocatalysts, such as porphyrin [5] and  $\text{g-C}_3\text{N}_4$  [6,

7], have been extensively studied and show significant performance improvement via rational molecular design. However, porphyrin has a valence band edge potential (V.B. = ca. 1.0 V) [8,9] not sufficient enough to oxidize organic pollutants; while  $\text{g-C}_3\text{N}_4$  exhibits a band gap (ca. 2.7 eV) [10] too wide to absorb much portion of the solar spectrum.

Perylene diimide (PDI) supramolecular, recently reported by our group, overcomes the main drawbacks mentioned in porphyrin and  $\text{g-C}_3\text{N}_4$ . It exhibits both a narrow bandgap (< 2 eV) and a high valence band edge potential for oxidation (V.B. = ca. 1.6 V) [11–13]. PDI showed considerably degrading activity for dye and phenolic pollutants, better than the well-known photocatalysts, such as  $\text{g-C}_3\text{N}_4$  and  $\text{Bi}_2\text{WO}_6$ . However, charge localization effects, widely existed in organic semiconductors, hinder the charge transfer in PDI, leading to a high recombination rate and limiting the activity. Some prior work attempted to optimize the charge transfer processes via molecular design strategy, such as complex-cation introduction (i.e. Co-PDI [14]) or amine group

\* Corresponding authors at: Key Laboratory of Synthetic and Biological Colloids, Ministry of Education, School of Chemical and Material Engineering, Jiangnan University, Wuxi, Jiangsu, 214122, China.

E-mail addresses: [cpans@jiangnan.edu.cn](mailto:cpans@jiangnan.edu.cn) (C. Pan), [zhuyf@mail.tsinghua.edu.cn](mailto:zhuyf@mail.tsinghua.edu.cn) (Y. Zhu).

<https://doi.org/10.1016/j.apcatb.2021.120762>

Received 7 May 2021; Received in revised form 24 September 2021; Accepted 25 September 2021

Available online 28 September 2021

0926-3373/© 2021 Elsevier B.V. All rights reserved.

substitution (i.e.  $-\text{N}(\text{CH}_2)_2\text{-COOH}$  and  $-\text{N}(\text{CH}_2)_{10}\text{-COOH}$  [12]), and successfully enhanced PDI's activity. But the activity is still far from necessity, by considering that degrading 5 ppm phenol needs 3 h in the best reported cases [15].

Notably, PDI prepared in literatures, mainly exhibits a  $\pi$ -stacking interaction between aromatic rings. The formed  $\pi$ -stacked structure would be less effective for charge transfer relative to an in-plane  $\pi$ -conjugated structure because the latter, in principle, exhibits much higher delocalization of electrons. If we could expand the in-plane  $\pi$ -conjugated structure by controlling the corresponding crystal facet, the activity of PDI photocatalysts will be substantially enhanced. Besides that, PDI is known as a hole-driven photocatalyst, indicating the exposure of surfaces preferring holes may efficiently improve the reaction rate. Furthermore, holes captured by organic pollutants are multiple steps, which are considered tens of times slower relative to electrons captured by  $\text{O}_2$  reduction to form superoxide radicals (one-electron step) [16,17]. Therefore, the exposure ratio of the surfaces preferring holes may be as large as possible. In this sense, PDI nanosheets with  $\pi$ -conjugated preferential planes exposed will be the most promising candidates benefiting for the activity. However, such crystal facet control in a PDI photocatalyst has yet to be achieved.

Controlling photocatalysts with a suitable preferential orientation or to expose highly active lattice planes has been found effectively to accelerate charge transfer and decrease bandgap, and thus, benefits for the photocatalytic activity. The strategy has been tested to be valid in many inorganic semiconductors, such as  $\text{BiVO}_4$  [18,19],  $\text{Ta}_3\text{N}_5$  [20,21],  $\text{SrTiO}_3$  [22,23] and  $\text{BiOCl}$  [24]. The strategy, however, has been rarely applied to an organic photocatalytic system. Until recently, Wang et al. [25] reported that in polytriazine imide (PTI) photocatalyst, exposing  $\{10\text{--}10\}$  planes greatly enhanced the internal electric field, leading to promotion of charge transfer and highly efficient overall water splitting. But the photocatalyst responses mainly to a UV region ( $<400\text{ nm}$ ) and the exposure ratio of  $\{10\text{--}10\}$  planes are only 82%. The application of the strategy to a wide-spectrum-responsive photocatalyst like PDI and further increasing the exposure ratio up to 100% in the system are, therefore, much of interest, with respect to the efficient utilization of solar spectra.

In this paper, PDI nanosheets ( $\pi$ -conjugated-PDI) with nearly 100% exposure of  $\pi$ -conjugated planes were reported for the first time. The structure and structure-related photocatalytic activity was studied by comparing with anisotropic PDI nanoparticles exposing with (020) planes and PDI nanorods ( $\pi$ -stacked-PDI) exposing with  $\pi$ -stacked planes.  $\pi$ -conjugated-PDI exhibits excellent photocatalytic activity among the three samples on degrading phenols, 8–17 times higher than those in reported PDI photocatalysts [11,12]. The origin of the high activity is revealed by spectroscopic and PEC measurements and DFT calculation. In our previous study, we built a large external dipole for enhancing the internal electric field in inorganic semiconductors [26]. However, in this work, we found facet control in organic semiconductors is another effective method for enhancing the internal electric field. Effects of preferentially exposed  $\pi$ -conjugated planes on the enhancement of the internal electric field, and the improvement of the charge separation and transfer are discussed in details. The current research may not only be cooperative with other PDI modification methods to obtain higher activity, but also show some guidelines for the design and development of more efficient narrow-bandgap organic photocatalysts.

## 2. Experimental section

### 2.1. Synthesis of PDI with preferentially exposing various planes

Commercial 3,4,9,10-Perylenetetracarboxylic Diimide (PDI) was purchased from Alfa Aesar Chemical Reagent Co., Ltd (Shanghai, China). All other chemicals (AR class) were purchased from National Chemical company (Shanghai, China) and used without further purification. Ultrapure water (18.20 M $\Omega$ ) was used in all experiments.

#### 2.1.1. Synthesis of $\pi$ -conjugated-PDI

$\pi$ -conjugated-PDI was prepared by an ethylene glycol (EG)-induced self-assembly method. Typically, 0.1 g Commercial-PDI was dissolved in 20 mL concentrated sulfuric acid (ca. 98 wt%) via sonication to form a red solution. The solution was rapidly poured into a 200 mL ethylene glycol (EG) aqueous solution (25 vol%) under stirring. The formative red suspension was further stirred for 15 min and left alone for another 45 min to allow PDI molecules having sufficient time to achieve self-assembly. PDI precipitates were collected by filtration with a 0.45  $\mu\text{m}$  ultrafilter membrane and washed several times till pH = 7. The obtained sample was finally dried overnight at 60  $^\circ\text{C}$ . The sample was named as  $\pi$ -conjugated-PDI because it exhibited a nanosheet structure with preferentially exposing  $\pi$ -conjugated planes (detailed in the results and discussion part).

#### 2.1.2. Synthesis of $\pi$ -stacked-PDI

$\pi$ -stacked-PDI was prepared by a water-induced self-assembly method, according to our previous reported [11]. Typically, 0.1 g Commercial-PDI was dissolved in 20 mL concentrated sulfuric acid and then, rapidly poured into 100 mL water under stirring. The subsequent washing and collection steps are similar as above. Note that we slightly modified our previous method by changing the water and acid ratio in order to obtain a regular morphology for easily studying the exposing surface. The sample was named as  $\pi$ -stacked-PDI because it exhibited a nanorod structure with preferentially exposing  $\pi$ -stacked planes (detailed in the results and discussion part).

#### 2.1.3. Synthesis of Anisotropic-PDI

Anisotropic-PDI was prepared by a ball milling method. Typically, 0.1 g Commercial-PDI together with stainless beads was ball-milled at 1400 rpm for 30 min. The red PDI powders were found to be partially stuck to jar walls or left on the bottom. The sample was collected by scratching with spatulas and 70% was obtained. The obtained PDI was named as Anisotropic-PDI because the sample was nanoparticles with several planes exposed (detailed in the results and discussion part).

### 2.2. Characterization of the materials

X-ray diffraction (XRD) patterns were recorded on a D8 X-ray diffractometer with a Cu target as a radiation source (Bruker AXS, German). Transmission electron microscopy (TEM) images were collected on a JEM-2100 transmission electron microscope (JEOL, Japan) with an acceleration voltage of 200 kV. Fourier-transform infrared (FT-IR) spectra was recorded on a Nicolet 6700 spectrometer (Thermo, USA) equipped with an Attenuated total reflectance (ATR) accessory. Raman spectra were recorded on an in via spectrometer (Renishaw, UK). X-ray photoelectron spectroscopy (XPS) measurements were carried out with an AXIS Supra (Kratos, UK) using monochromatized Al K $\alpha$  radiation ( $h\nu = 1486.6\text{ eV}$ , 225 W) as the X-ray source and all spectra were calibrated with C 1 s (284.8 eV). UV–vis diffuse reflectance spectra (UV-DRS) were obtained on a UV-3600 spectrophotometer (Shimadzu, Japan). Steady-state fluorescence (FL) spectra were recorded on a FS5 spectrophotometer (PL, Edinburgh, UK). The surface photovoltage (SPV) measurement was carried out with a solid junction photovoltaic cell (ITO/sample/ITO) using light source-monochromator-lock-in detection technique [27].

### 2.3. Photodegradation of phenols

Photocatalytic performance was evaluated by degradation of 5 ppm phenols (phenol, catechol, BPA, 4-CP or 2,4-DCP) under visible light (300 W Xe lamp, 420 nm cut-off filter, Perfect Light, Beijing, China). The average light intensity was measured to be 90 mW/cm $^2$  by a PL-MW 2000 photo radiometer (Perfect Light, Beijing, China). Before reaction, 25 mg PDI photocatalyst was dispersed in 50 mL phenols solution via 5 min sonication and then kept in dark for another 40 min under stirring to

achieve the equilibrium of adsorption and desorption. The adsorption capacity of PDI photocatalyst for phenol, catechol, 4-CP or 2,4-DCP is less than 5%, while the adsorption capacity for BPA is ca. 15%. During the reaction, the suspension was irradiated with the Xe lamp, and maintained at  $25 \pm 2^\circ\text{C}$  with cooling water to prevent thermal effects. The concentration of the pollutant was measured by extracting 0.5 mL reaction solution with a syringe topped with a  $0.45\ \mu\text{m}$  syringe filter every 20 min, and monitored by a high performance liquid chromatography (HPLC, JASCO, Japan) equipping with a C18 reversed phase column (mobile phase, MeOH:  $\text{H}_2\text{O}$  = 70: 30 vol%; flow rate,  $1\ \text{mL min}^{-1}$ ). The concentration of the phenolic pollutants was calculated based on the absorbance at 270 nm.

#### 2.4. Photoelectrochemical measurements

Transient photocurrent and electrochemical impedance spectroscopy (EIS) were measured on a CHI-750E electrochemical workstation (Chenhua, Shanghai, China). Three-electrode system was employed for these studies, which contained a PDI/FTO glass ( $1.5 \times 1\ \text{cm}^2$ ) as a working electrode, a platinum net as a counter electrode ( $1.5 \times 1.5\ \text{cm}^2$ ), and a standard Ag/AgCl electrode ( $E_{\text{Ag/AgCl}} = 0.210\ \text{V}$  vs. NHE) as a reference electrode.  $0.1\ \text{M Na}_2\text{SO}_4$  was used as an electrolyte. A 300 W Xe lamp was used as a light source. EIS responses of the photocatalysts were measured at the frequencies ranging from 0.01 to 100000 Hz in parallel with the alternating current signal amplitude of 5 mV.

The PDI/FTO working electrode was prepared as follows: 5.0 mg

prepared PDI was dispersed in an ethanol and n-hexane mixed solution ( $50\ \mu\text{L} + 50\ \mu\text{L}$ ). The obtained suspension was uniformly cast onto a  $1.5 \times 1\ \text{cm}^2$  FTO glass by dropping. The PDI/FTO electrode was obtained by calcination at  $300^\circ\text{C}$  for 30 min in air.

### 3. Results and discussion

#### 3.1. 100% exposure ratio of $\pi$ -conjugated planes achieved on PDI photocatalysts

The exposed lattice planes on various PDI prepared and the morphology related were investigated by TEM and AFM, and correlated by crystal schematics. (Fig. 1 and Supporting Information Figs. 1–3).

$\pi$ -conjugated-PDI was prepared by a solvent-induced self-assembly method. In TEM (Fig. 1a and Supporting Information Fig. S1 a & b) and AFM figures (Fig. 1b),  $\pi$ -conjugated-PDI exhibits a nanosheet structure with dimensions of ca.  $1.5\ \mu\text{m}$  in length, ca.  $1.0\ \mu\text{m}$  in width and ca. 4.3 nm in thickness.

Exposed lattice planes on the prepared PDI nanosheets is clarified by HRTEM (Fig. 1a inset). The figure shows a clear lattice spacing of 0.324 nm, which corresponds to a (122) plane of a PDI crystal. Note that the planes observed in the HRTEM should be vertical to exposed planes in most cases [24,28]. As a result, the exposed planes for  $\pi$ -conjugated-PDI nanosheets are deduced to be ( $\bar{1}12$ ), a lattice plane primarily dominated by the  $\pi$ -conjugated backbone. Fig. 1c and Supporting Information Fig. S2b gives the geometric relationship between the

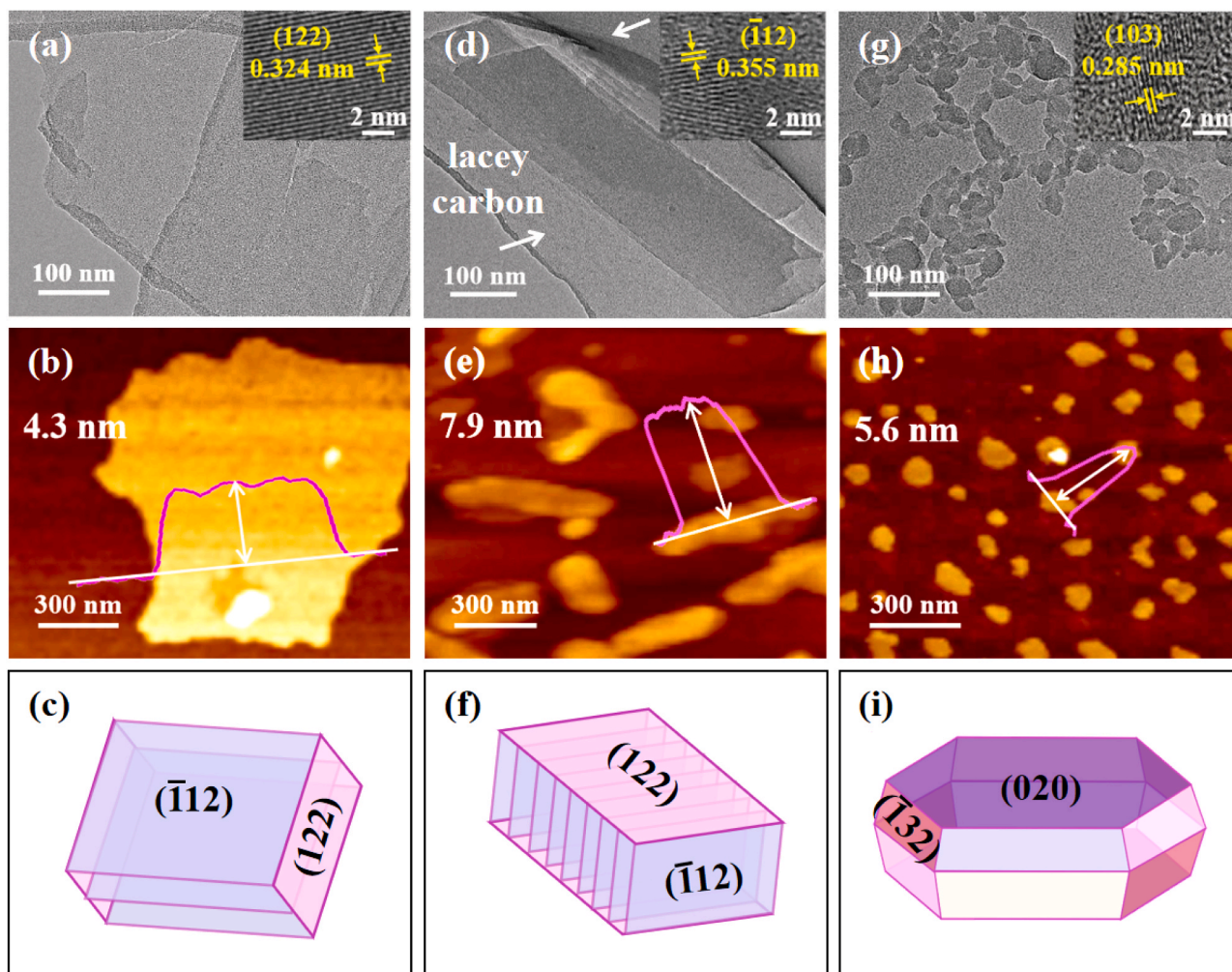


**Fig. 1.** TEM (a), AFM(b) and crystal schematics (c) of  $\pi$ -conjugated-PDI; TEM (d), AFM(e) and crystal schematics (f) of  $\pi$ -stacked-PDI; and TEM (g), AFM(h) and crystal schematics (i) of Anisotropic-PDI. Fig. 1a, d and g insets are the concurrent HRTEM.



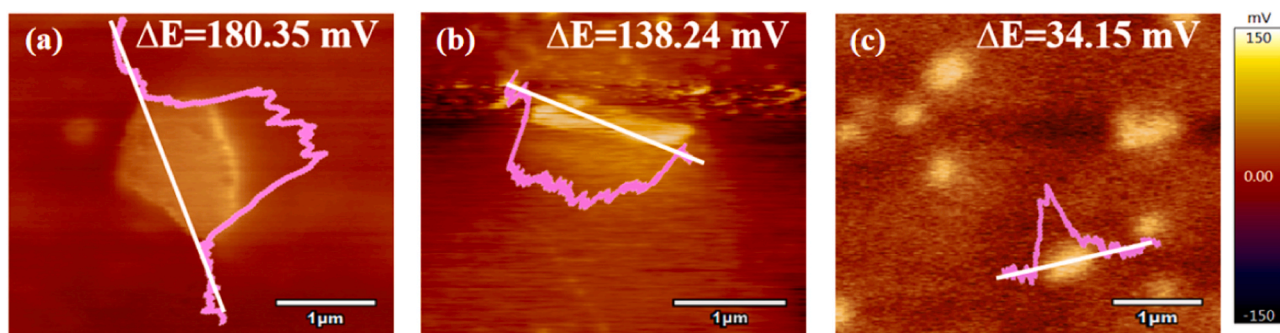


Fig. 2. Surface potentials of  $\pi$ -conjugated-PDI (a),  $\pi$ -stacked-PDI (b), and Anisotropic-PDI (c).

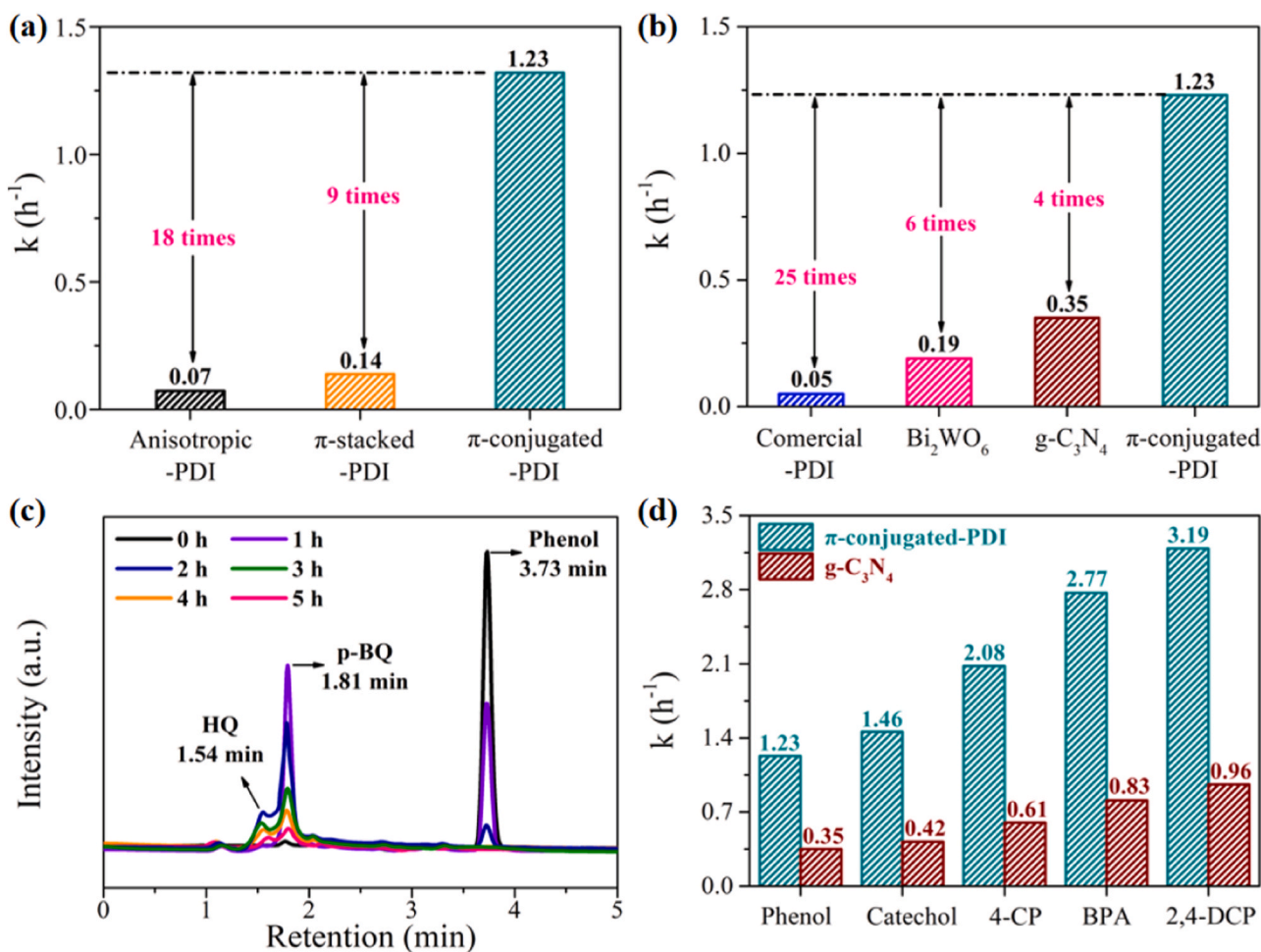


Fig. 3. (a) Phenol photodegradation on  $\pi$ -conjugated-PDI,  $\pi$ -stacked-PDI and Anisotropic-PDI. (b) Phenol photodegradation on  $\pi$ -conjugated-PDI, Commercial-PDI, and other well-known photocatalysts, Bi<sub>2</sub>WO<sub>6</sub> and g-C<sub>3</sub>N<sub>4</sub>. (c) HPLC chromatograms of phenol degradation process on  $\pi$ -conjugated-PDI. (d) Various phenols (phenol, catechol, 4-CP, BPA, 2,4-DCP) degradation on  $\pi$ -conjugated-PDI and g-C<sub>3</sub>N<sub>4</sub>. (Xe lamp with a 420 nm cut-off filter, 25 mg photocatalyst, 50 mL H<sub>2</sub>O, 5 ppm phenols).

exposed  $\pi$ -conjugated ( $-112$ ) planes and the observed (122) planes. According to the geometric relationship, the exposure ratio of  $\pi$ -conjugated ( $-112$ ) planes on PDI nanosheets is estimated to be ca. 99.3% (detailed in Supporting Information Fig. S3a).

For comparison,  $\pi$ -stacked-PDI was prepared by a water-induced self-assembly method according to our previous reported [11], while Anisotropic-PDI was prepared by a ball milling method. The relationship between the morphology and the exposed planes on  $\pi$ -stacked-PDI and Anisotropic-PDI are studied similarly as we did for  $\pi$ -conjugated-PDI (Fig. 1d–f and g–i, Supporting Information Fig. S1c & d, Fig. S1e & f). For  $\pi$ -stacked-PDI, a nanorod structure is observed, having dimensions of ca.

600 nm in length, ca. 150 nm in width and ca. 7.9 nm in thickness; while for Anisotropic-PDI, nanoparticle structure is observed, having dimensions of ca. 70 nm in diameter and ca. 5.6 nm in thickness.

The exposed planes on  $\pi$ -stacked-PDI and Anisotropic-PDI are revealed by HRTEM. For  $\pi$ -stacked-PDI, HRTEM (Fig. 1d inset) shows a lattice spacing of 0.355 nm, consistent with the  $\pi$ -conjugated plane ( $-112$ ), indicating  $\pi$ -stacked-PDI nanorods are formed as we reported, by the stacking of  $\pi$ -conjugated planes [11]. In this case, exposed planes on  $\pi$ -stacked-PDI may be (122) planes, as deduced from the geometric relationship shown in Fig. 1f and Supporting Information Fig. S2b. On the other hand, for Anisotropic-PDI, the lattice spacing is found to

0.285 nm, corresponding to (103) planes (Fig. 1g inset) on PDI crystals, indicating the exposed top and bottom planes are (020) planes (Supporting Information Fig. S2c). The exposed planes on the edge are also determined by HRTEM as shown in Supporting Information Fig. S1e inset. In this case, the lattice spacing of 0.296 nm indicates that the exposed surface on the edge is ( $\bar{1}$ 32) planes (Fig. 1i, Supporting Information Fig. S1e inset and Fig. S2d). Although some percentages of ( $\bar{1}$ 32) planes is found to expose on the edge, the major planes exposed on Anisotropic-PDI may still be (020) planes by considering the large difference between the diameter and thickness of the observed particles. (020) planes have also been reported to expose for PDI particles in the literature [29]. We then calculated the exposure ratio of  $\pi$ -conjugated planes for  $\pi$ -stacked-PDI and Anisotropic-PDI, according to the geometric relationship shown in Fig. 1f & i and Supporting Information Fig. S3b & c, for comparison to that in  $\pi$ -conjugated-PDI. In those cases, the exposure ratio of  $\pi$ -conjugated planes for  $\pi$ -stacked-PDI and Anisotropic-PDI is estimated to be ca. 1.2% and 0%, respectively, much smaller relative to that for  $\pi$ -conjugated PDI (ca. 99.3%).

The exposure ratio and size difference of  $\pi$ -conjugated planes leads to the different  $\pi$ - $\pi$  interaction for  $\pi$ -conjugated-PDI,  $\pi$ -stacked-PDI and Anisotropic-PDI. The  $\pi$ - $\pi$  interaction can be revealed by the Raman and XPS spectra as shown in Supporting Information Fig. S4 & 5, respectively. In Raman spectra, the difference of peak intensity ratio between C=C stretching vibration ( $1592\text{ cm}^{-1}$ ) and C-H bending vibration ( $1324\text{ cm}^{-1}$ ) in the PDI's skeleton is due to the variation of  $\pi$ - $\pi$  interaction [30]. In our case, the ratios are 1.74, 1.67 and 1.51 for  $\pi$ -conjugated-PDI,  $\pi$ -stacked-PDI and Anisotropic-PDI, respectively. The results indicate that  $\pi$ -conjugated-PDI has the strongest  $\pi$ - $\pi$  interaction effect, while Anisotropic-PDI has the weakest  $\pi$ - $\pi$  interaction effect. On the other hand, in XPS spectra, the binding energy of C=O peak is reported to be inversely proportional to the  $\pi$ - $\pi$  interaction [31]. In our case, the binding energy of C=O peak of three types of PDI changes as follows: Anisotropic-PDI (288.0 eV) >  $\pi$ -stacked-PDI (287.8 eV) >  $\pi$ -conjugated-PDI (287.5 eV). This indicates that  $\pi$ -conjugated-PDI exhibits the strongest  $\pi$ - $\pi$  interaction effect, which is consistent with our Raman results.

The difference in exposed planes and morphology may also influence the preferential orientation in the PDI crystals, and can be detected by XRD. In Supporting Information Fig. S6, XRD peak ratios between  $\pi$ - $\pi$  stacking peaks (Peak B and Peak C locating between  $25^\circ$  and  $28^\circ$ ) and the strongest peak (Peak A locating at  $12^\circ$ ) change with the change of preferential planes in three types of PDI (Supporting Information Table S1) [11,32]. Taking  $I_B/I_A$  as an example (the tendency of  $I_C/I_A$  is similar), the ratio changes in a sequence as follows:  $\pi$ -conjugated-PDI ( $I_B/I_A = 0.55$ ) >  $\pi$ -stacked-PDI ( $I_B/I_A = 0.42$ ) > Anisotropic-PDI ( $I_B/I_A = 0.38$ ). The highest ratio suggests that  $\pi$ -conjugated planes (Peak B) are not only exposed planes, but also the preferential planes in  $\pi$ -conjugated-PDI. The lowest ratio suggests that (020) planes (Peak A, the strongest peak) are both the exposed and preferential planes in Anisotropic-PDI in a similar conclusion. In the case of  $\pi$ -stacked-PDI, the ratio is reduced by ca. 25% relative to that in  $\pi$ -conjugated-PDI, and thus the preferential  $\pi$ -conjugated planes may decrease accordingly.

XRD patterns further show that all the peaks of  $\pi$ -conjugated-PDI,  $\pi$ -stacked-PDI and Anisotropic-PDI are consistent with standard PDI, indicating that there is negligible crystal structure change during the preparation process. Elemental analysis (EA) confirms that there is slight difference for C, H and N contents between  $\pi$ -conjugated-PDI,  $\pi$ -stacked-PDI, Anisotropic-PDI and Commercial-PDI ( $\text{C}_{24}\text{H}_{10}\text{O}_4\text{N}_2$ ) (Supporting Information Table S2). Both XRD and EA results indicate that PDI with different  $\pi$ -conjugated surfaces exposed are formed only by physical rearrangements of molecules, rather than chemical reactions. In previous reports, both J-PDI and H-PDI are controllable prepared with different alkyl group N-substitution or bay-substitution [12]. But in our case, no such substitution is performed for all three types of PDI. Therefore, all three types of PDI will exhibit H-type aggregation, the most commonly observed aggregation for unsubstituted PDI [29,33].

Among these PDI photocatalysts, the formation process of  $\pi$ -conjugated-PDI is focused on as it is our target material. Solvent-induced effect of EG is suggested to help to form the material. FTIR spectra were employed to reveal the effect of EG. Supporting Information Fig. S7 shows the FTIR spectra of  $\pi$ -conjugated-PDI,  $\pi$ -conjugated-PDI+EG, and EG. In the figure, an absorption peak emerges at around  $3200\text{--}3400\text{ cm}^{-1}$ , which can be attributed to the O-H stretching vibration peak. In the case of EG, the O-H peak appears at  $3283\text{ cm}^{-1}$ , while in the case of  $\pi$ -conjugated-PDI+EG, the peak shifts to a lower wave-number ( $3271\text{ cm}^{-1}$ ) and becomes wider compared to the case of EG. Notably  $\pi$ -conjugated-PDI does not show any O-H peak, indicating the above observed peak shift and shape change are not due to the peak overlap between EG and PDI. The peak shift and shape change observed in  $\pi$ -conjugated-PDI+EG may be due to the formation of new intermolecular H-bonds ( $\text{O-H}\cdots\text{N}$ ) between EG and PDI, and leading to a decrease of O-H vibration energy. The H-bonding between PDI and EG may facilitate in-plane  $\pi$ -conjugated self-assembly and lead to the formation of the observed PDI nanosheets. The effect of H-bonding on the formation of  $\pi$ -conjugated structure is reported in former literatures on self-assembly of layered graphene [34,35].

As mentioned above, we successfully prepared  $\pi$ -conjugated-PDI nanosheets. BET specific surface area of  $\pi$ -conjugated-PDI is  $9.5\text{ m}^2/\text{g}$ , in the same order of magnitude as that of reported  $\pi$ -stacked-PDI [12].  $\pi$ -conjugated-PDI nanosheets mainly expose  $\pi$ -conjugated planes, with an exposure ratio of 99.3%. The exposure ratio is much higher than  $\pi$ -stacked-PDI we reported previously [12] and also, in top ranking by referring literatures,  $\text{TiO}_2$  micro crystals (47%) [36],  $\text{BiOCl}$  nanosheets (80%) [24] and  $\text{WO}_3$  nanocrystals (91%) [37]. Nearly 100% exposure ratio has been once highlighted for  $\text{TiO}_2$  nanosheets and  $\text{BiOBr}$  micro-flower, and leads to remarkably performance enhancement [38,39]. In our case, a 100% exposure ratio of  $\pi$ -conjugated planes may benefit for the charge separation and transfer and thus, improve the photocatalytic activity. See below for detailed discussions.

### 3.2. High exposure ratio of $\pi$ -conjugated planes for largely enhancing the internal electric field

We next studied the effect of preferentially exposed planes of various PDI on the internal electric field as well as energy band structure, -two key factors that may influence the activity.

The effect of preferentially exposed planes on the internal electric field are shown in Fig. 2, Supporting Information Table S3 and Fig. S8 & 9. The internal electric field are reported to be proportional to the square root of the product of surface potential and surface charge density [40, 41]. Surface potential can be tested by the Kelvin probe force microscopy (KPFM), while surface charge density may be proportional to the Zeta potential [42]. Fig. 2 shows the surface potentials ( $\Delta E$ ) of  $\pi$ -conjugated-PDI,  $\pi$ -stacked-PDI and Anisotropic-PDI measured by KPFM. The measured potentials are  $185.51 \pm 14.06\text{ mV}$ ,  $126.38 \pm 11.86\text{ mV}$  and  $34.17 \pm 3.05\text{ mV}$ , respectively.  $\pi$ -conjugated-PDI with preferentially exposed  $\pi$ -conjugated planes exhibits the highest surface potential among three types of PDI. Zeta potentials of three types of PDIs are shown in Supporting Information Table S3. The measured zeta potential changes in a sequence as follows:  $\pi$ -conjugated-PDI ( $-65.3\text{ mV}$ ) >  $\pi$ -stacked-PDI ( $-58.8\text{ mV}$ ) > Anisotropic-PDI ( $-45.9\text{ mV}$ ).  $\pi$ -conjugated-PDI with preferentially exposed  $\pi$ -conjugated planes, again, exhibits the largest Zeta potential, indicating the highest surface charge density. Both KPFM and Zeta potential measurement suggest that preferential  $\pi$ -conjugated planes exposed on  $\pi$ -conjugated-PDI will enhance the internal electric field more efficiently than other preferential planes exposed on  $\pi$ -stacked-PDI and Anisotropic-PDI.

The internal electric field is also quantitatively reflected by the product of the photo-generated charge density and open circuit potential (OCP) [43]. Supporting Information Fig. S8a-c shows the photo-generated charge densities of  $\pi$ -conjugated-PDI,  $\pi$ -stacked-PDI and Anisotropic-PDI are  $69.085\text{ }\mu\text{C}/\text{cm}^2$ ,  $22.758\text{ }\mu\text{C}/\text{cm}^2$  and  $11.542$

$\mu\text{C}/\text{cm}^2$ , respectively, according to transient photocurrent measurement. Supporting Information Fig. S8d shows the OCP of  $\pi$ -conjugated-PDI,  $\pi$ -stacked-PDI and Anisotropic-PDI are 0.18 V, 0.07 V and 0.03 V, respectively. Accordingly, the internal electric field of  $\pi$ -conjugated-PDI is 2.80 and 6.01 times higher than those of  $\pi$ -stacked-PDI and Anisotropic-PDI, respectively (Supporting Information Fig. S9).

The effect of preferentially exposed planes on band absorption and band edge positions of three types of PDIs are studied as well. Supporting Information Fig. S10a shows the absorption edges are 730 nm, 722 nm, and 690 nm for  $\pi$ -conjugated-PDI,  $\pi$ -stacked-PDI and Anisotropic-PDI, respectively.  $\pi$ -conjugated-PDI exhibits the longest absorption wavelength, probably due to the highest  $\pi$ -conjugation degree originating from its large preferentially exposed  $\pi$ -conjugated planes [44]. The effect of preferentially exposed planes on the band edge positions are shown in Supporting Information Fig. S10b. According to the band gap (Supporting Information Fig. S10a Inset) and Mott-Schottky (Supporting Information Fig. S11) measurements,  $E_{\text{CB}}$  of  $\pi$ -conjugated-PDI,  $\pi$ -stacked-PDI and Anisotropic-PDI are found to be  $-0.10$ ,  $-0.15$  and  $-0.33$  V (vs. NHE), respectively; while  $E_{\text{VB}}$  are found to be 1.65, 1.62 and 1.48 V (vs. NHE), respectively. The change tendency of  $E_{\text{CB}}$  and  $E_{\text{VB}}$  suggests that PDI with larger  $\pi$ -conjugated planes exposing exhibit a more positive shift of the band edge. This will give  $\pi$ -conjugated-PDI stronger oxidation capability.

$\pi$ -conjugated-PDI exhibits much stronger built-in electric field relative to  $\pi$ -stacked-PDI and Anisotropic-PDI, and also the most positive valence band edge potential, because it exposes the highest ratio of  $\pi$ -conjugated planes. The exposure of specific crystal planes has been reported to influence the electronic structure in many photocatalysts, such as layered  $\text{Bi}_3\text{O}_4\text{Cl}$  nanosheets [45] and  $\text{TiO}_2$  [46]. In our case, high exposure ratio of  $\pi$ -conjugated planes may also lead to the suitable electronic structure for facilitating the charge separation and transfer, and significantly improve the photocatalytic performance, as reported in literatures [42,47] (detailed in the DFT calculation part).

### 3.3. High exposure ratio of $\pi$ -conjugated planes for boosting the photodegradation of phenols

Phenol is used as a model pollutant to evaluate the photocatalytic activity of PDI exposed of different planes. The pollutant is often found in the wastewater and regarded as one of the most toxic and hard to degrade aromatic compounds [48].

The phenol degradation rates on various PDI are shown in Fig. 3a. Under visible light ( $\lambda \geq 420$  nm) irradiation, phenol-degradation rate constants ( $k$ ) of  $\pi$ -conjugated-PDI,  $\pi$ -stacked-PDI and Anisotropic-PDI are  $1.23 \text{ h}^{-1}$ ,  $0.14 \text{ h}^{-1}$ ,  $0.07 \text{ h}^{-1}$ , respectively.  $\pi$ -conjugated-PDI shows the highest activity, which is ca. 18 times and 9 times as high as that of Anisotropic-PDI and  $\pi$ -stacked-PDI, respectively. In particular,  $\pi$ -conjugated-PDI degrades 91% of phenol within 2 h irradiation, while  $\pi$ -stacked-PDI and Anisotropic-PDI degrade only 25% and 14% of phenol, respectively, within the same time.

Fig. 3b shows the comparison of phenol degradation on  $\pi$ -conjugated-PDI, Commercial-PDI and other reported highly-efficient visible-light photocatalysts,  $\text{Bi}_2\text{WO}_6$  and  $\text{g-C}_3\text{N}_4$ .  $\text{Bi}_2\text{WO}_6$  and  $\text{g-C}_3\text{N}_4$  were prepared according to our previous reported [49,50]. In the figure, kinetic rate constants of  $\pi$ -conjugated-PDI, Commercial-PDI,  $\text{Bi}_2\text{WO}_6$  and  $\text{g-C}_3\text{N}_4$ , are found to be  $1.23 \text{ h}^{-1}$ ,  $0.05 \text{ h}^{-1}$ ,  $0.19 \text{ h}^{-1}$  and  $0.35 \text{ h}^{-1}$ , respectively. Clearly,  $\pi$ -conjugated-PDI shows the best activity, that is, ca. 25 times, 6 times and 4 times as high as that of Commercial-PDI,  $\text{Bi}_2\text{WO}_6$  and  $\text{g-C}_3\text{N}_4$ , respectively. Most notably,  $\pi$ -conjugated-PDI with preferentially exposed  $\pi$ -conjugated planes shows the highest activity among all the PDI-based photocatalysts and in a top level among the visible-light-responsive organic photocatalysts (Supporting Information Table S4 & 5).

Fig. 3c shows the intermediates of phenol degradation monitored by HPLC. Three peaks locating at 3.73 min, 1.81 min and 1.54 min are observed, respectively. They can be assigned as phenol, p-benzoquinone

(p-BQ), and hydroquinone (HQ), respectively, by using external standard methods. In the initial 1 h, the peak area of phenol gradually decreased from 5.0 ppm to about 1.6 ppm; while the peak areas of p-BQ and HQ increased from 0 to 2.1 ppm and 0.5 ppm, respectively. With the irradiation time increasing, the concentrations of phenol, p-BQ, and HQ all decreased. Phenol peak disappeared in about 2 h, while p-BQ and HQ peaks disappeared after 5 h. Supporting Information Fig. S12 shows the total organic carbon (TOC) removal curve of  $\pi$ -conjugated-PDI. The results show that phenol can be eventually converted into  $\text{CO}_2$  and  $\text{H}_2\text{O}$  after 5 h irradiation. It is noted that the phenol degradation pathway on  $\pi$ -conjugated-PDI is similar to the reported PDI [44], indicating that exposing  $\pi$ -conjugated planes will not affect the degradation mechanism.

The main oxidative species involving in the degradation process is revealed by the trapping experiments. Supporting Information Fig. S13a shows the results of radical-capturing experiments during the phenol degradation on  $\pi$ -conjugated PDI. The addition of t-BuOH, a  $\bullet\text{OH}$  scavenger [2,51], slightly decreases the activity; the addition of p-BQ, a  $\bullet\text{O}_2^-$  scavenger [2,12], moderately decreases the activity; and most notably, the addition of KI, a hole scavenger [51], dramatically decreases the activity. The effect of various scavengers on the activity indicates that holes are the main active species during the phenol degradation. The result is also supported by our EPR observation (Supporting Information Fig. S13b). Here N-hydroxyphthalimide was used for capturing holes as reported [52,53] (detailed in Supporting Information Section S1.3). In the experiment, a triplet signal is observed. The signal can be assigned as phthalimide-N-oxyl radicals generated by holes on the photocatalyst according to the literature [54], indicating holes generated on  $\pi$ -conjugated-PDI are the main oxidative species.

The stability of the photocatalytic activity of  $\pi$ -conjugated-PDI is then evaluated. The results show that  $\pi$ -conjugated-PDI exhibits negligible activity decreases after 5 cycles (Supporting Information Fig. S14). FTIR and XRD are recorded before and after the experiments to test if there are any structural changes (Supporting Information Fig. S15). Negligible structure change is observed, indicating the structure is stable. Both the recycling experiments and structure characterizations suggest that the preferentially exposed  $\pi$ -conjugated planes are stable during the photodegradation.

Next various phenols are used in the  $\pi$ -conjugated-PDI photocatalytic system, aiming to evaluate the selectivity (Fig. 3d).  $\text{g-C}_3\text{N}_4$  is listed as a control, which is prepared as we reported [50]. In this case, phenols degradation activity on  $\pi$ -conjugated-PDI are  $1.23 \text{ h}^{-1}$  for phenol,  $1.46 \text{ h}^{-1}$  for catechol,  $2.08 \text{ h}^{-1}$  for 4-CP,  $2.77 \text{ h}^{-1}$  for BPA, and  $3.19 \text{ h}^{-1}$  for 2,4-DCP, while the activity of degrading concurrent phenols pollutants on  $\text{g-C}_3\text{N}_4$  is  $0.35 \text{ h}^{-1}$ ,  $0.42 \text{ h}^{-1}$ ,  $0.61 \text{ h}^{-1}$ ,  $0.83 \text{ h}^{-1}$ ,  $0.96 \text{ h}^{-1}$ , respectively. Clearly,  $\pi$ -conjugated-PDI shows about 3–4 times as high as that of  $\text{g-C}_3\text{N}_4$ , indicating that the excellent performance of  $\pi$ -conjugated-PDI originates from the preferentially exposed  $\pi$ -conjugated plane, not from the special interaction between phenol and the photocatalyst.

Antibiotics like Tetracycline (TC) and Ciprofloxacin (CIP) are also used for evaluating the photodegradation capability of our  $\pi$ -conjugated-PDI, as shown in Supporting Information Fig. S16a & b. In this case,  $\text{g-C}_3\text{N}_4$  is also listed as a control, as it does for phenols degradation. The results show that  $\pi$ -conjugated-PDI exhibits about 3–4 times of degradation rates for TC and CIP higher than those of  $\text{g-C}_3\text{N}_4$ , respectively, similar as what we observed for phenols.

### 3.4. Activity enhancement mechanism with high exposure ratio of $\pi$ -conjugated planes

The excellent photocatalytic performance of  $\pi$ -conjugated-PDI is probably due to the strong internal electric field and positive valence band edge potential caused by the preferentially exposed  $\pi$ -conjugated planes as we discussed in the Section 3.2. Both of the properties will result in high exciton dissociation, rapid charge separation and transfer.



The relationship between preferentially exposed planes and photo-generated charges is further clarified by PL spectra and photoelectrochemical (PEC) measurements as shown below.

The influence of preferentially exposed planes on the PDI's exciton lifetime is shown by transient PL spectra [55] (Fig. 4a and Supporting Information Table S6). The results exhibit that the decay of exciton in a sequence as follows:  $\pi$ -conjugated-PDI (1.57 ns) >  $\pi$ -stacked-PDI (1.06 ns) > Anisotropic-PDI (0.60 ns). According to the literature, photocatalytic reaction requires excitons to diffuse into the PDI/pollutant solution interface within their lifetime, and to dissociate into photo-generated charges [56]. The longest exciton lifetime of  $\pi$ -conjugated-PDI indicates that  $\pi$ -conjugated planes exposed is more conducive to driving the photocatalytic reaction by producing more photo-generated charges relative to (122) exposed on  $\pi$ -stacked-PDI and (020) planes exposed on Anisotropic-PDI.

The de-excitation rate of the exciton can be reflected by steady-state PL spectroscopy [57]. Fig. 4b exhibits PL intensities of three types of PDI. In the figure,  $\pi$ -conjugated-PDI shows the lowest intensity, while Anisotropic-PDI shows the highest intensity. The low PL intensity is reported to indicate the efficient exciton dissociation to produce photo-generated charges [56]. Moreover, Peumans et al. [58] reported that in CuPc-PTCDI, the n-type doping (incomplete purification) of PTCDI enhanced the internal electric field, leading to promote the dissociation of exciton into photo-generated charges. In our case, the PL results indicate that  $\pi$ -conjugated planes exhibit the strong internal electric-field and thus facilitate exciton dissociation into photo-generated charges.

Photo-generated charge separation and transfer on preferentially

exposed planes can be further reflected from SPV spectra (Fig. 4c). SPV is reported to be caused by the surface charge concentration originating from the photo-generated charge transferring to the surface [27]. In the figure, Anisotropic-PDI exhibits the lowest SPV signal (43.4  $\mu$ V); while  $\pi$ -conjugated-PDI exhibits the highest one (120.4  $\mu$ V). The highest signal indicates that preferentially exposed  $\pi$ -conjugated planes clearly benefit for the separation and transfer of photo-generated charge, which is consistent with the PL results.

Fig. 4d shows the measured EIS results and fitting curves for three types of PDI with different planes preferentially exposed (detailed in Supporting Information Table S7). The inset figure is the equivalent circuit used, in which  $R_s$  represents the solution resistance;  $R_{ct}$  represents the charge transfer resistance; and CPE represents the constant phase element for the electrolyte/electrode interface. The equivalent circuit has been verified in the Urea-PDI system [42]. In our case, the semicircle radius of  $\pi$ -conjugated-PDI,  $\pi$ -stacked-PDI and Anisotropic-PDI under irradiation are much smaller than those in dark, respectively, indicating a large number of charge are generated. Among them, the radii of  $\pi$ -conjugated-PDI is the smallest, indicating that  $\pi$ -conjugated planes will reduce the charge transfer resistance the most efficiently in all the preferentially exposed planes obtained [59].

Above all, the PL and PEC results indicate that preferentially exposed  $\pi$ -conjugated planes will facilitate exciton dissociation and charge separation and transfer, and thus lead to a remarkable activity enhancement. In order to understand the origin of the promotion of charge separation and transfer on  $\pi$ -conjugated planes relative to other obtained exposed planes ((122) and (020) planes), the charge density difference, electrostatic potentials, and surface energy ( $\gamma$ ) of PDI was

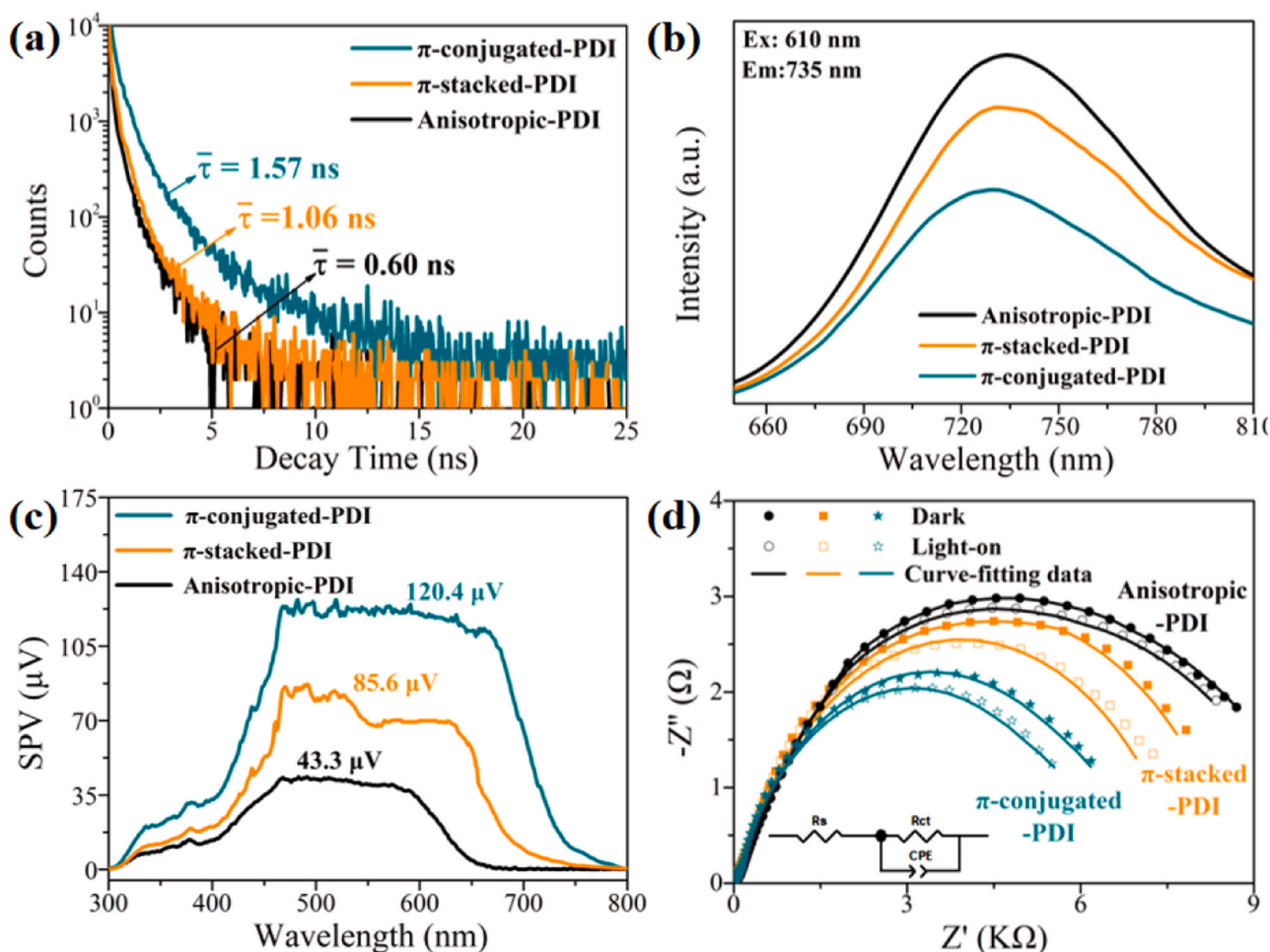


Fig. 4. Transient PL spectra (a), steady-state PL spectra (b), SPV spectra (c), and the EIS spectra (d) of  $\pi$ -conjugated-PDI,  $\pi$ -stacked-PDI and Anisotropic-PDI.

calculated by DFT.

Fig. 5a-c shows the charge density difference on different crystal planes, ( $\bar{1}12$ ), (122) and (020). ( $\bar{1}12$ ), (122) and (020) are the preferential planes exposed on  $\pi$ -conjugated-PDI,  $\pi$ -stacked-PDI, and Anisotropic-PDI, respectively, according to our results from Fig. 1. The figure shows that the charge density on  $\pi$ -conjugated ( $\bar{1}12$ ) planes is the highest, while on (020) planes is the lowest. The large electron density will increase potential between the planes [60] and thus cause a strong electric field as reported in literatures [19,61]. The internal electric field will lead to an efficient charge separation in  $\pi$ -conjugated-PDI [62,63]. Holes are supposed to maintain on the  $\pi$ -conjugated surface due to a large electron density; while electrons are supposed to prefer transferring to the edge. The supposed charge separation is demonstrated by corresponding phase spectra of SPV spectra of  $\pi$ -conjugated-PDI and the facet-selective photo-deposition experiments. For the corresponding SPV phase spectra of  $\pi$ -conjugated-PDI, phase angle occurs at the range of  $-30^\circ$  to  $-5^\circ$ , which means that holes are staying on the surface according to literatures [64] (Supporting Information Fig. S17). In the case of photo-deposition experiments, tiny Pt particles are found at the edges of  $\pi$ -conjugated-PDI during the photo-generated electron-induced deposition (Supporting Information Fig. S18a & b); while tiny  $\text{MnO}_2$  particles are found on the  $\pi$ -conjugated surface during the hole-induced deposition (Supporting Information Fig. S18c & d). These results support our hypothesis that due to the existence of the internal electric field, photo-generated electrons and holes are spatially separated and transferred to (122) and  $\pi$ -conjugated ( $\bar{1}12$ ) facets, respectively. The large electron density also means a high atom density and will enhance the work function [65] on the plane, leading to a high band edge potential. The strong electric field and high band edge potential will benefit for the charge separation and transfer as well as the photocatalytic activity [47,66].

Fig. 5d-f shows the calculated electrostatic potentials within ( $\bar{1}12$ ), (122) and (020) planes. The potential changes in a following sequence:  $\pi$ -conjugated ( $\bar{1}12$ ) planes (1.7 eV) < (122) planes (5.1 eV) < (020) planes (6.0 eV). The electrostatic potential reflects the difficulty level for

charge transfer on the given crystal plane. Accordingly,  $\pi$ -conjugated ( $\bar{1}12$ ) planes exhibit the easiest charge transfer due to the lowest electrostatic potential with this crystal plane [25].

Supporting Information Fig. S19 and Table S8 listed the  $\gamma$  calculated based on ( $\bar{1}12$ ), (122) and (020) planes.  $\gamma$  of ( $\bar{1}12$ ), (122) and (020) planes are  $2.42 \text{ J/m}^2$ ,  $0.51 \text{ J/m}^2$  and  $0.24 \text{ J/m}^2$ , respectively.  $\pi$ -conjugated ( $\bar{1}12$ ) plane exhibits the highest  $\gamma$ , indicating it is the most active for producing oxidative species used for photodegradation, as reported in  $\text{Ag}_3\text{PO}_4$  [67],  $\text{TiO}_2$  [46]. The DFT calculation results show that  $\pi$ -conjugated ( $\bar{1}12$ ) planes may be good for the charge separation, transfer and the production of oxidative species and thus, promote the activity.

Combining PEC and PL results with the DFT calculation,  $\pi$ -conjugated planes improve the photocatalytic activity of PDI, probably due to the following reasons: (1)  $\pi$ -conjugated planes possess large electron density and thus exhibit a strong internal electric field and valence band edge potential, which can effectively separate and transfer photo-generated charge; (2)  $\pi$ -conjugated planes exhibit the lowest in-plane electrostatic potential and benefit for the charge transfer; (3)  $\pi$ -conjugated planes have the largest  $\gamma$  and thus, facilitate the production of active species for photodegradation.

#### 4. Conclusion

In conclusion,  $\pi$ -conjugated-PDI nanosheets with nearly 100%  $\pi$ -conjugated planes exposed have been first prepared by a solvent-induced self-assembly method. The high exposure ratio of  $\pi$ -conjugated planes on PDI nanosheets leads to excellent phenol degradation activity ( $1.23 \text{ h}^{-1}$ ), 8–17 times higher than reported PDI. The high exposure ratio of  $\pi$ -conjugated planes is found to efficiently promote the internal electric field and thus facilitate the charge separation and transfer, enhancing the activity. The work helps us understand the facet-dependent activity of organic photocatalysts with wide spectrum response, and may also promote the development of high-activity organic photocatalysts for environmental remediation.

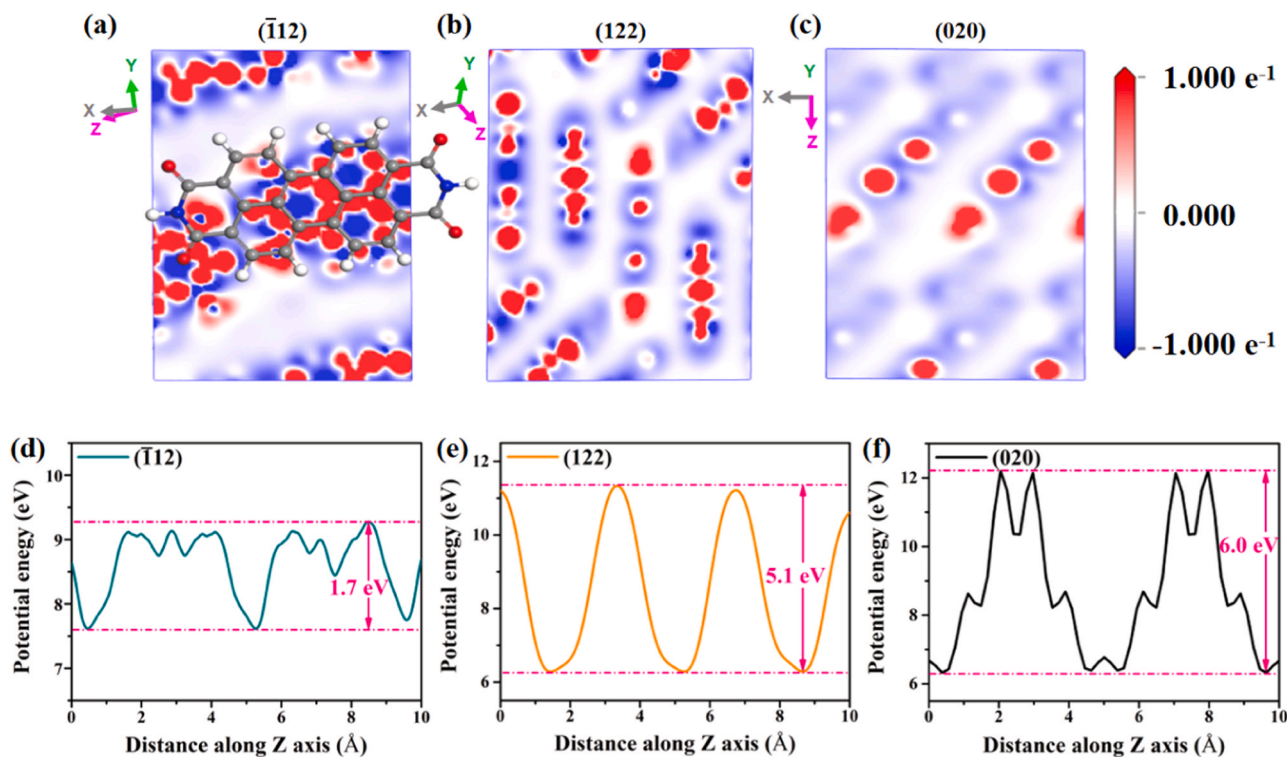


Fig. 5. (a-c) Charge density difference on ( $\bar{1}12$ ), (122) and (020) planes of PDI. (d-f) Electrostatic potentials within ( $\bar{1}12$ ), (122) and (020) planes. ( $\bar{1}12$ ) is the  $\pi$ -conjugated plane; (122) is the  $\pi$ -stacked plane; and (020) is the generally exposed plane.



## CRediT authorship contribution statement

**Yaning Zhang:** Conceptualization, Methodology, Writing - original draft; **Dan Wang:** Validation, Investigation; **Weixu Liu:** Investigation; **Yang Lou:** Visualization, Investigation; **Ying Zhang:** Formal analysis, Data curation; **Yuming Dong:** Methodology, Formal analysis; **Jing Xu:** Methodology, Investigation; **Chengsi Pan:** Methodology, Investigation, Software, Writing – review & editing, Supervision; **Yongfa Zhu:** Writing - review & editing, Supervision.

## Declaration of Competing Interest

The authors report no declarations of interest.

## Acknowledgements

This work was supported by the National Natural Science Foundation of China (22172065, 21908079, 21676123, 21902009, 21707052), Natural Science Foundation of Jiangsu Province (BK20201345, BK20211239), Startup Funding at Jiangnan University (1045210322190170, 1045281602190010, 1042050205204100, 1045219039200010, 1045219032210020), the State Key Laboratory of Fine Chemicals, Dalian University of Technology (KF2005), Fundamental Research Funds for the Central Universities (JUSRP52004B, JUSRP12033), Jiangsu Agriculture Science and Technology Innovation Fund (CX(20)3108).

## Appendix A. Supporting information

Supplementary data associated with this article can be found in the online version at [doi:10.1016/j.apcatb.2021.120762](https://doi.org/10.1016/j.apcatb.2021.120762).

## References

- [1] W.H.M. Abdelraheem, M.K. Patil, M.N. Nadagouda, D.D. Dionysiou, Hydrothermal synthesis of photoactive nitrogen- and boron-codoped TiO<sub>2</sub> nanoparticles for the treatment of bisphenol A in wastewater: synthesis, photocatalytic activity, degradation byproducts and reaction pathways, *Appl. Catal. B Environ.* 241 (2019) 598–611, <https://doi.org/10.1016/j.apcatb.2018.09.039>.
- [2] Q. Gao, J. Xu, Z. Wang, Y. Zhu, Enhanced visible photocatalytic oxidation activity of perylene diimide/g-C<sub>3</sub>N<sub>4</sub> n-n heterojunction via  $\pi$ - $\pi$  interaction and interfacial charge separation, *Appl. Catal. B Environ.* 271 (2020), 118933, <https://doi.org/10.1016/j.apcatb.2020.118933>.
- [3] L. Jiang, X. Yuan, G. Zeng, Z. Wu, J. Liang, X. Chen, L. Leng, H. Wang, H. Wang, Metal-free efficient photocatalyst for stable visible-light photocatalytic degradation of refractory pollutant, *Appl. Catal. B Environ.* 221 (2018) 715–725, <https://doi.org/10.1016/j.apcatb.2017.09.059>.
- [4] Z. Zhu, W. Guo, Y. Zhang, C. Pan, J. Xu, Y. Zhu, Y. Lou, Research progress on methane conversion coupling photocatalysis and thermocatalysis, *Carbon Energy* (2021) 1–22, <https://doi.org/10.1002/cey2.127>.
- [5] Z. Zhang, Y. Zhu, X. Chen, H. Zhang, J. Wang, A full-spectrum metal-free porphyrin supramolecular photocatalyst for dual functions of highly efficient hydrogen and oxygen evolution, *Adv. Mater.* 31 (2019), 1806626, <https://doi.org/10.1002/adma.201806626>.
- [6] M. Zhang, X. Wang, Two dimensional conjugated polymers with enhanced optical absorption and charge separation for photocatalytic hydrogen evolution, *Energy Environ. Sci.* 7 (2014) 1902–1906, <https://doi.org/10.1039/C3EE44189J>.
- [7] Y. Kang, Y. Yang, L.C. Yin, X. Kang, G. Liu, H.M. Cheng, An amorphous carbon nitride photocatalyst with greatly extended visible-light-responsive range for photocatalytic hydrogen generation, *Adv. Mater.* 27 (2015) 4572–4577, <https://doi.org/10.1002/adma.201501939>.
- [8] J. Wang, L. Xu, T. Wang, R. Li, Y. Zhang, J. Zhang, T. Peng, Porphyrin conjugated polymer grafted onto BiVO<sub>4</sub> nanosheets for efficient Z-scheme overall water splitting via cascade charge transfer and single-atom catalytic sites, *Adv. Energy Mater.* 11 (2021), 2003575, <https://doi.org/10.1002/aenm.202003575>.
- [9] J. Xu, Q. Gao, Z. Wang, Y. Zhu, An all-organic OD/2D supramolecular porphyrin/g-C<sub>3</sub>N<sub>4</sub> heterojunction assembled via  $\pi$ - $\pi$  interaction for efficient visible photocatalytic oxidation, *Appl. Catal. B Environ.* 291 (2021), 120059, <https://doi.org/10.1016/j.apcatb.2021.120059>.
- [10] L. Shi, L. Yang, W. Zhou, Y. Liu, L. Yin, X. Hai, H. Song, J. Ye, Photoassisted construction of holey defective g-C<sub>3</sub>N<sub>4</sub> photocatalysts for efficient visible-light-driven H<sub>2</sub>O<sub>2</sub> production, *Small* 14 (2018), 1701342, <https://doi.org/10.1002/sml.201703142>.
- [11] D. Liu, J. Wang, X. Bai, R. Zong, Y. Zhu, Self-assembled PDINH supramolecular system for photocatalysis under visible light, *Adv. Mater.* 28 (2016) 7284–7290, <https://doi.org/10.1002/adma.201601168>.
- [12] J. Wang, D. Liu, Y. Zhu, S. Zhou, S. Guan, Supramolecular packing dominant photocatalytic oxidation and anticancer performance of PDI, *Appl. Catal. B Environ.* 231 (2018) 251–261, <https://doi.org/10.1016/j.apcatb.2018.03.026>.
- [13] J. Yang, H. Miao, W. Li, H. Li, Y. Zhu, Designed synthesis of a p-Ag<sub>2</sub>S/n-PDI self-assembled supramolecular heterojunction for enhanced full-spectrum photocatalytic activity, *J. Mater. Chem. A* 7 (2019) 6482–6490, <https://doi.org/10.1039/C9TA00580C>.
- [14] Z. Zhong, R. Li, W. Lin, X. Xu, L. Kang, One-dimensional nanocrystals of cobalt perylene diimide polymer with in-situ generated FeOOH for efficient photocatalytic water oxidation, *Appl. Catal. B Environ.* 260 (2020), 118135, <https://doi.org/10.1016/j.apcatb.2019.118135>.
- [15] J. Yang, H. Miao, J. Jing, Y. Zhu, W. Choi, Photocatalytic activity enhancement of PDI supermolecular via  $\pi$ - $\pi$  action and energy level adjusting with graphene quantum dots, *Appl. Catal. B Environ.* 281 (2021), 119547, <https://doi.org/10.1016/j.apcatb.2020.119547>.
- [16] L. Zhang, H.H. Mohamed, R. Dillert, D. Bahnemann, Kinetics and mechanisms of charge transfer processes in photocatalytic systems: A review, *J. Photochem. Photobiol. C* 13 (2012) 263–276, <https://doi.org/10.1016/j.jphotochem.2012.07.002>.
- [17] M.W. Kanan, D.G. Nocera, In situ formation of an oxygen-evolving catalyst in neutral water containing phosphate and Co<sup>2+</sup>, *Science* 321 (2008) 1072–1075, <https://doi.org/10.1126/science.1162018>.
- [18] Q. Wang, K. Domen, Particulate photocatalysts for light-driven water splitting: mechanisms, challenges, and design strategies, *Chem. Rev.* 120 (2020) 919–985, <https://doi.org/10.1021/acs.chemrev.9b00201>.
- [19] R. Li, F. Zhang, D. Wang, J. Yang, M. Li, J. Zhu, X. Zhou, H. Han, C. Li, Spatial separation of photogenerated electrons and holes among {010} and {110} crystal facets of BiVO<sub>4</sub>, *Nat. Commun.* 4 (2013) 1432, <https://doi.org/10.1038/ncomms2401>.
- [20] C. Zhou, J. Zhou, L. Lu, J. Wang, Z. Shi, B. Wang, L. Pei, S. Yan, Y. Zhentao, Z. Zou, Surface electric field driven directional charge separation on Ta<sub>3</sub>N<sub>5</sub> cuboids enhancing photocatalytic solar energy conversion, *Appl. Catal. B Environ.* 237 (2018) 742–752, <https://doi.org/10.1016/j.apcatb.2018.06.036>.
- [21] Z. Shi, J. Feng, H. Shan, X. Wang, Z. Xu, H. Huang, Q. Qian, S. Yan, Z. Zou, Low onset potential on single crystal Ta<sub>3</sub>N<sub>5</sub> polyhedral array photoanode with preferential exposure of {001} facets, *Appl. Catal. B Environ.* 237 (2018) 665–672, <https://doi.org/10.1016/j.apcatb.2018.06.037>.
- [22] T. Takata, J. Jiang, Y. Sakata, M. Nakabayashi, N. Shibata, V. Nandal, K. Seki, T. Hisatomi, K. Domen, Photocatalytic water splitting with a quantum efficiency of almost unity, *Nature* 581 (2020) 411–414, <https://doi.org/10.1038/s41586-020-2278-9>.
- [23] X. Wu, X. Wang, J. Li, G. Zhang, Boosting molecular oxygen activation of SrTiO<sub>3</sub> by engineering exposed facets for highly efficient photocatalytic oxidation, *J. Mater. Chem. A* 5 (2017) 23822–23830, <https://doi.org/10.1039/C7TA08061A>.
- [24] J. Jiang, K. Zhao, X. Xiao, L. Zhang, Synthesis and facet-dependent photoreactivity of BiOCl single-crystalline nanosheets, *J. Am. Chem. Soc.* 134 (2012) 4473–4476, <https://doi.org/10.1021/ja210484t>.
- [25] L. Lin, Z. Lin, J. Zhang, X. Cai, W. Lin, Z. Yu, X. Wang, Molecular-level insights on the reactive facet of carbon nitride single crystals photocatalysing overall water splitting, *Nat. Catal.* 3 (2020) 649–655, <https://doi.org/10.1038/s41929-020-0476-3>.
- [26] C. Pan, Z. Wang, Y. Lou, Y. Zhang, Y. Dong, Y. Zhu, The construction of a wide-spectrum-responsive and high-activity photocatalyst, Bi<sub>25</sub>CoO<sub>40</sub>, via the creation of large external dipoles, *J. Mater. Chem. A* 9 (2021) 3616–3627, <https://doi.org/10.1039/D0TA11549E>.
- [27] T.F. Xie, D.J. Wang, L.J. Zhu, T.J. Li, Y.J. Xu, Application of surface photovoltage technique in photocatalysis studies on modified TiO<sub>2</sub> photo-catalysts for photo-reduction of CO<sub>2</sub>, *Mater. Chem. Phys.* 70 (2001) 103–106, [https://doi.org/10.1016/S0254-0584\(00\)00475-2](https://doi.org/10.1016/S0254-0584(00)00475-2).
- [28] J. Yang, Q. Li, H. Zu, Z. Yang, W. Qu, M. Li, H. Li, Surface-engineered sponge decorated with copper selenide for highly efficient gas-phase mercury immobilization, *Environ. Sci. Technol.* 54 (2020) 16195–16203, <https://doi.org/10.1021/acs.est.0c04982>.
- [29] X. Cao, Y. Wu, H. Fu, J. Yao, Self-assembly of perylene diimide nanobelts and their size-tunable exciton dynamic properties, *J. Phys. Chem. Lett.* 2 (2011) 2163–2167, <https://doi.org/10.1021/jz2009488>.
- [30] R. Singh, E. Giussani, M.M. Mróz, F. Di Fonzo, D. Fazzi, J. Cabanillas-González, L. Oldridge, N. Vaenas, A.G. Kontos, P. Falaras, A.C. Grimsdale, J. Jacob, K. Müllen, P.E. Keivanidis, On the role of aggregation effects in the performance of perylene-diimide based solar cells, *Org. Electron.* 15 (2014) 1347–1361, <https://doi.org/10.1016/j.orgel.2014.03.044>.
- [31] H. Miao, J. Yang, G. Peng, H. Li, Y. Zhu, Enhancement of the degradation ability for organic pollutants via the synergistic effect of photoelectrocatalysis on a self-assembled perylene diimide (SA-PDI) thin film, *Sci. Bull.* 64 (2019) 896–903, <https://doi.org/10.1016/j.scib.2019.05.006>.
- [32] J. Yang, H. Miao, Y. Wei, W. Li, Y. Zhu,  $\pi$ - $\pi$  Interaction between self-assembled perylene diimide and 3D graphene for excellent visible-light photocatalytic activity, *Appl. Catal. B Environ.* 240 (2019) 225–233, <https://doi.org/10.1016/j.apcatb.2018.09.003>.
- [33] F. Würthner, Perylene bisimide dyes as versatile building blocks for functional supramolecular architectures, *Chem. Commun. (Camb.)* (2004) 1564–1579, <https://doi.org/10.1039/b401630k>.
- [34] M. Lotya, Y. Hernandez, P.J. King, R.J. Smith, Y. Nicolosi, L.S. Karlsson, F. M. Blighe, S. De, Z. Wang, I.T. McGovern, Liquid phase production of graphene by exfoliation of graphite in surfactant/water solutions, *J. Am. Chem. Soc.* 131 (2009) 3611–3620, <https://doi.org/10.1021/ja807449u>.

- [35] S. Wang, L. Yang, Q. Wang, Y. Fan, J. Shang, S. Qiu, J. Li, W. Zhang, X. Wu, Supramolecular self-assembly of layer-by-layer graphene film driven by the synergism of  $\pi$ - $\pi$  and hydrogen bonding interaction, *J. Photochem. Photobiol. A* 355 (2018) 249–255, <https://doi.org/10.1016/j.jphotochem.2017.09.023>.
- [36] H.G. Yang, C.H. Sun, S.Z. Qiao, J. Zou, G. Liu, S.C. Smith, H.M. Cheng, G.Q. Lu, Anatase TiO<sub>2</sub> single crystals with a large percentage of reactive facets, *Nature* 453 (2008) 638–641, <https://doi.org/10.1038/nature06964>.
- [37] D. Zhang, S. Wang, J. Zhu, H. Li, Y. Lu, WO<sub>3</sub> nanocrystals with tunable percentage of (001)-facet exposure, *Appl. Catal. B Environ.* 123–124 (2012) 398–404, <https://doi.org/10.1016/j.apcatb.2012.04.049>.
- [38] K. Chen, Z. Jiang, J. Qin, Y. Jiang, R. Li, H. Tang, X. Yang, Synthesis and improved photocatalytic activity of ultrathin TiO<sub>2</sub> nanosheets with nearly 100% exposed (001) facets, *Ceram. Int.* 40 (2014) 16817–16823, <https://doi.org/10.1016/j.ceramint.2014.07.050>.
- [39] J. Sun, X. Li, Q. Zhao, B. Liu, Ultrathin nanoflake-assembled hierarchical BiOBr microflower with highly exposed {001} facets for efficient photocatalytic degradation of gaseous ortho-dichlorobenzene, *Appl. Catal. B: Environ.* 281 (2021), 119478, <https://doi.org/10.1016/j.apcatb.2020.119478>.
- [40] T. Kanata-Kito, M. Matsunaga, H. Takakura, Y. Hamakawa, T. Nishino, F.H. Pollak, M. Cardona, D.E. Aspnes, Photoreflectance characterization of built-in potential in MBE-produced as-grown GaAs surface, *Proc. SPIE* 1286 (1990) 56–65, <https://doi.org/10.1117/12.20837>.
- [41] G. Morello, F. Della Sala, L. Carbone, L. Manna, G. Maruccio, R. Cingolani, M. De Giorgi, Intrinsic optical nonlinearity in colloidal seeded grown CdSe/CdS nanostructures: photoinduced screening of the internal electric field, *Phys. Rev. B* 78 (2008), 195313, <https://doi.org/10.1103/PhysRevB.78.195313>.
- [42] Z. Zhang, X. Chen, H. Zhang, W. Liu, W. Zhu, Y. Zhu, A highly crystalline perylene imide polymer with the robust built-in electric field for efficient photocatalytic water oxidation, *Adv. Mater.* 32 (2020), 1907746, <https://doi.org/10.1002/adma.201907746>.
- [43] J. Li, L. Cai, J. Shang, Y. Yu, L. Zhang, Giant enhancement of internal electric field boosting bulk charge separation for photocatalysis, *Adv. Mater.* 28 (2016) 4059–4064, <https://doi.org/10.1002/adma.201600301>.
- [44] J. Wang, W. Shi, D. Liu, Z. Zhang, Y. Zhu, D. Wang, Supramolecular organic nanofibers with highly efficient and stable visible light photooxidation performance, *Appl. Catal. B Environ.* 202 (2017) 289–297, <https://doi.org/10.1016/j.apcatb.2016.09.037>.
- [45] J. Li, L. Zhang, Y. Li, Y. Yu, Synthesis and internal electric field dependent photoreactivity of Bi<sub>2</sub>O<sub>4</sub>Cl single-crystalline nanosheets with high {001} facet exposure percentages, *Nanoscale* 6 (2014) 167–171, <https://doi.org/10.1039/C3NR05246J>.
- [46] Y. Li, K.-A. Min, B. Han, L.Y.S. Lee, Ni nanoparticles on active (001) facet-exposed rutile TiO<sub>2</sub> nanopillar arrays for efficient hydrogen evolution, *Appl. Catal. B: Environ.* 282 (2021), 119548, <https://doi.org/10.1016/j.apcatb.2020.119548>.
- [47] J. Li, G. Zhan, Y. Yu, L. Zhang, Superior visible light hydrogen evolution of Janus bilayer junctions via atomic-level charge flow steering, *Nat. Commun.* 7 (2016) 11480, <https://doi.org/10.1038/ncomms11480>.
- [48] A. Barrera, F. Tzompantzi, J.M. Padilla, J.E. Casillas, G. Jácome-Acatitla, M. E. Cano, R. Gómez, Reusable PdO/Al<sub>2</sub>O<sub>3</sub>-Nd<sub>2</sub>O<sub>3</sub> photocatalysts in the UV photodegradation of phenol, *Appl. Catal. B Environ.* 144 (2014) 362–368, <https://doi.org/10.1016/j.apcatb.2013.07.024>.
- [49] H. Fu, L. Zhang, W. Yao, Y. Zhu, Photocatalytic properties of nanosized Bi<sub>2</sub>WO<sub>6</sub> catalysts synthesized via a hydrothermal process, *Appl. Catal. B Environ.* 66 (2006) 100–110, <https://doi.org/10.1016/j.apcatb.2006.02.022>.
- [50] J. Xu, Z. Wang, Y. Zhu, Enhanced visible-light-driven photocatalytic disinfection performance and organic pollutant degradation activity of porous g-C<sub>3</sub>N<sub>4</sub> nanosheets, *ACS Appl. Mater. Interfaces* 9 (2017) 27727–27735, <https://doi.org/10.1021/acsami.7b07657>.
- [51] P. Qiu, C. Xu, H. Chen, F. Jiang, X. Wang, R. Lu, X. Zhang, One step synthesis of oxygen doped porous graphitic carbon nitride with remarkable improvement of photo-oxidation activity: role of oxygen on visible light photocatalytic activity, *Appl. Catal. B Environ.* 206 (2017) 319–327, <https://doi.org/10.1016/j.apcatb.2017.01.058>.
- [52] E. Baciocchi, M. Bietti, M.D. Fusco, O. Lanzalunga, A kinetic study of the electron-transfer reaction of the phthalimide-N-oxyl radical (PINO) with ferrocenes, *J. Org. Chem.* 72 (2007) 8748–8754, <https://doi.org/10.1021/jo071211q>.
- [53] B.B. Wentzel, M.P.J. Donners, P.L. Alsters, M.C. Feiters, R.J.M. Nolte, N-Hydroxyphthalimide/Cobalt(II) catalyzed low temperature benzylic oxidation using molecular oxygen, *Cheminform* 56 (2000) 7797–7803, [https://doi.org/10.1016/S0040-4020\(00\)00679-7](https://doi.org/10.1016/S0040-4020(00)00679-7).
- [54] C. Zhang, Z. Huang, J. Lu, N. Luo, F. Wang, Generation and confinement of long-lived N-Oxyl radical and its photocatalysis, *J. Am. Chem. Soc.* 140 (2018) 2032–2035, <https://doi.org/10.1021/jacs.7b12928>.
- [55] J. Kong, W. Zhang, G. Li, D. Huo, Y. Guo, X. Niu, Y. Wan, B. Tang, A. Xia, Excited-state symmetry-breaking charge separation dynamics in multibranched perylene diimide molecules, *J. Phys. Chem. Lett.* 11 (2020) 10329–10339, <https://doi.org/10.1021/acs.jpclett.0c03210>.
- [56] T.M. Clarke, J.R. Durrant, Charge photogeneration in organic solar cells, *Chem. Rev.* 110 (2010) 6736–6767, <https://doi.org/10.1021/cr900271s>.
- [57] G.J. Hedley, A. Ruseckas, I.D. Samuel, Light harvesting for organic photovoltaics, *Chem. Rev.* 117 (2017) 796–837, <https://doi.org/10.1021/acs.chemrev.6b00215>.
- [58] A. Liu, S. Zhao, S.B. Rim, J. Wu, M. Könnemann, P. Erk, P. Peumans, Control of electric field strength and orientation at the donor–acceptor interface in organic solar cells, *Adv. Mater.* 20 (2008) 1065–1070, <https://doi.org/10.1002/adma.200702554>.
- [59] W. Dai, L. Jiang, J. Wang, Y. Pu, Y. Zhu, Y. Wang, B. Xiao, Efficient and stable photocatalytic degradation of tetracycline wastewater by 3D Polyaniline/Perylene diimide organic heterojunction under visible light irradiation, *Chem. Eng. J.* 397 (2020), 125476, <https://doi.org/10.1016/j.cej.2020.125476>.
- [60] N. Bouhmaid, N.E. Ghermani, Advances in electric field and atomic surface derived properties from experimental electron densities, *Phys. Chem. Chem. Phys.* 10 (2008) 3934–3941, <https://doi.org/10.1039/b801741g>.
- [61] J. Zhu, F. Fan, R. Chen, H. An, Z. Feng, C. Li, Direct imaging of highly anisotropic photogenerated charge separations on different facets of a single BiVO<sub>4</sub> photocatalyst, *Angew. Chem. Int. Ed. Engl.* 54 (2015) 9111–9114, <https://doi.org/10.1002/anie.201504135>.
- [62] Q. Xu, L. Zhang, J. Yu, S. Wageh, A.A. Al-Ghamdi, M. Jaroniec, Direct Z-scheme photocatalysts: principles, synthesis, and applications, *Mater. Today* 21 (2018) 1042–1063, <https://doi.org/10.1016/j.mattod.2018.04.008>.
- [63] X. Li, C. Garlisi, Q. Guan, S. Anwer, K. Al-Ali, G. Palmisano, L. Zheng, A review of material aspects in developing direct Z-scheme photocatalysts, *Mater. Today* 47 (2021) 75–107, <https://doi.org/10.1016/j.mattod.2021.02.017>.
- [64] S. Li, Q. Zhao, D. Meng, D. Wang, T. Xie, Fabrication of metallic charge transfer channel between photoanode Ti/Fe<sub>2</sub>O<sub>3</sub> and cocatalyst CoO<sub>x</sub>: an effective strategy for promoting photoelectrochemical water oxidation, *J. Mater. Chem. A* 4 (2016) 16661–16669, <https://doi.org/10.1039/c6ta05337h>.
- [65] R.W. Strayer, Work function measurements of single crystal surfaces by the field emission retarding potential method, *Cryst. Field Theory* 1 (1973) 220–223, <https://doi.org/10.1109/SENSOR.1995.717148>.
- [66] Y. Zhu, X. Ma, Y. Xu, X. Chen, Large dipole moment induced efficient bismuth chromate photocatalysts for wide-spectrum driven water oxidation and complete mineralization of pollutants, *Natl. Sci. Rev.* 7 (2020) 652–659, <https://doi.org/10.1093/nsr/nwz198>.
- [67] Y. Bi, S. Ouyang, N. Umezawa, J. Cao, J. Ye, Facet effect of single-crystalline Ag<sub>3</sub>PO<sub>4</sub> sub-microcrystals on photocatalytic properties, *J. Am. Chem. Soc.* 133 (2011) 6490–6492, <https://doi.org/10.1021/ja2002132>.